CEBAF-PR-92-021

The N* Program at CEBAF

Volker D. Burkert
CEBAF, 12000 Jefferson Avenue, Newport News,
Virginia 23606, USA

Invited talk, presented at BARYONS 92, June 1-5, 1992, New Haven, Ct.

CONTINUOUS ELECTRON BEAM ACCELERATOR FACILITY

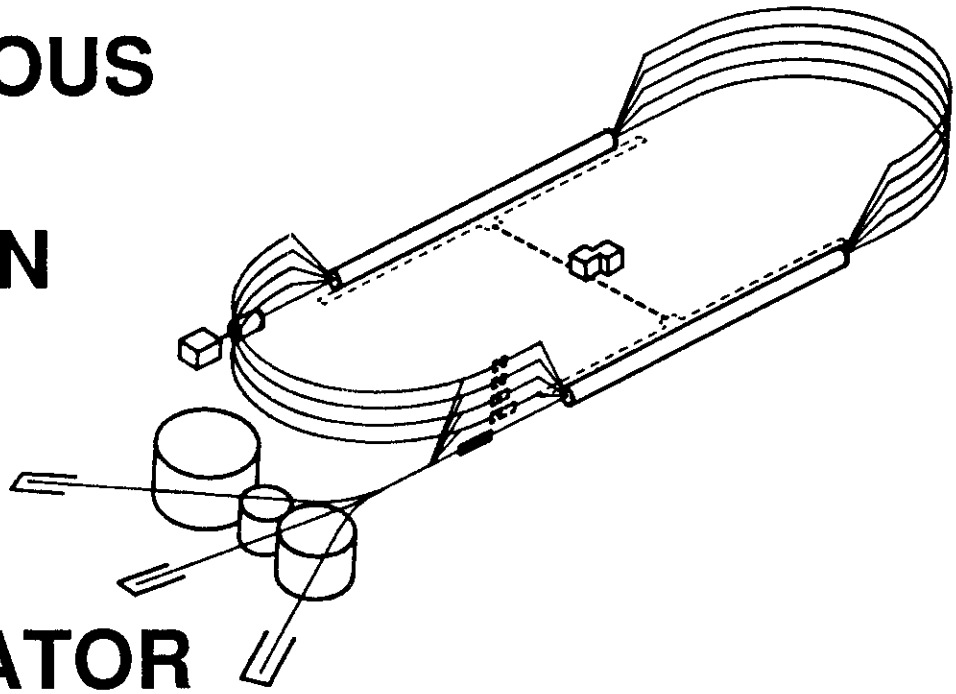

SURA *Southeastern Universities Research Association*

CEBAF
The Continuous Electron Beam Accelerator Facility

Newport News, Virginia

Copies available from:

Library
CEBAF
12000 Jefferson Avenue
Newport News
Virginia 23606

The Southeastern Universities Research Association (SURA) operates the Continuous Electron Beam Accelerator Facility for the United States Department of Energy under contract DE-AC05-84ER40150.

THE N* PROGRAM AT CEBAF

Volker D. Burkert *
CEBAF, 12000 Jefferson Avenue, Newport News,
Virginia 23606, USA

ABSTRACT

A brief summary of the experimental program at CEBAF to study electromagnetic transitions of nucleon resonances is given. The need for complete data sets, including measurements of polarization observables is stressed. It is emphasized that insight into fundamental properties of hadronic matter can be obtained by studying the Q^2 evolution of resonance transition amplitudes and their comparison with microscopic models of baryons.

1. Introduction

The process we are interested in studying is shown in Fig. 1. An electron is scattered off a nucleon, exchanges a virtual photon which transfers four-momentum to the nucleon. In doing so it excites the nucleon into a higher energy state. At the same time, since the photon is space-like it will probe the spatial structure of the transition, and since both the photon and nucleon carry spin, it also probes the spin-structure of the transition. If this process is studied at sufficiently small distances, the internal spatial and spin-structure is probed at the quark-gluon level. In this case, we will obtain information about the interaction responsible for confining quarks and gluons into hadrons.

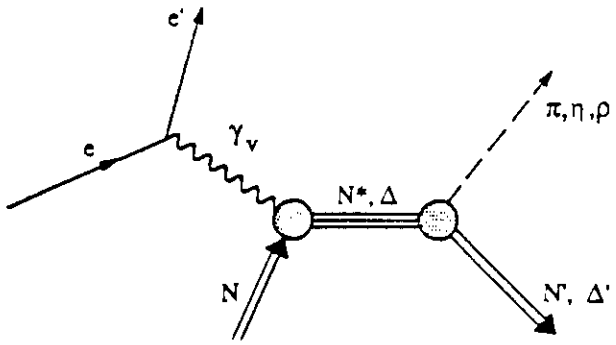

Fig. 1: Basic process of electromagnetic excitation of baryon resonances.

*Representing the CLAS N^* collaboration.

Fig. 2: Symmetric 3-quark arrangement versus diquark-quark arrangement.

To be more specific, some of the questions we may address are:

(1) What is the basic symmetry group underlying the structure of light-quark baryons? Does the SU(6) x O(3) symmetry group provide a realistic representation of the baryon structure, or are there different degrees of freedom that are relevant? For example, it is not at all clear which of the configurations depicted in Fig. 2 is more in accordance with the observed baryon spectrum. The symmetric 3-quark (q^3) picture is the most widely accepted one, however the diquark-quark ($q^2 - q$) picture has sufficiently many degrees of freedom to describe the observed light quark baryon spectrum, and it predicts a fewer number of unobserved states than the (q^3) picture.

(2) What role do gluonic degrees of freedom play in the baryon structure. Do they give rise to new spectroscopic states, and what is their influence on the internal structure of excited baryon states?

(3) If gluonic degrees of freedom do play an active role, what fraction of the angular momentum of excited baryon states is carried by the glue?

Fig. 3 shows the kinematical $Q^2 - \nu$ plane that can be studied using CEBAF's 4 GeV electron beam scattered on a proton target. Excited baryon states with masses in excess of 2.5 GeV are accessible. For the low mass states, such as the $P_{33}(1232)$, Q^2 values of up to 5 GeV^2 can be reached, which allows us to probe the internal structure at distances of 0.1 to 0.2 fermi.

The CEBAF Large Acceptance Spectrometer[1] (Fig. 4) will be used for most of the N^* program. CLAS is based on a toroidal magnet with six superconducting coils and allows detection of several particles in the final state. CLAS has been designed to operate in a high luminosity environment of $L \leq 10^{34}\ cm^{-2}s^{-1}$. For a large acceptance spectrometer, CLAS has good momentum and angular resolution, which allows employing the missing mass technique to identify one missing (typically neutral) particle in the final state, a feature that is particularly important in the N^* program. CLAS can be operated both with an electron beam and with an energy marked photon beam.

2. Goals of the N^* Program

The overall plan of the N* program is illustrated in Fig. 5. The primary experimental goal is to measure all accessible processes which are relevant to N* decays. Since none of these channels will come exclusively from resonance decays, non-resonant contribution have to be taken into account as well, and in some cases may even be dominant. While the physics of these non-resonant processes may be very interesting,

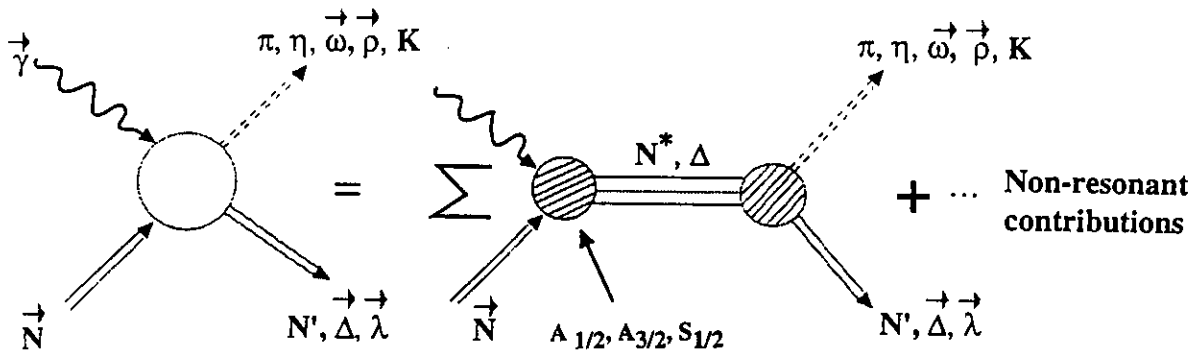

Fig. 5: Meson production and baryon resonance transitions with electromagnetic probes.

they are considered background for the purpose of this program. Extensive theoretical input is needed to eliminate the non-resonant components in the transition amplitudes, and to extract the photocoupling amplitudes $A_{1/2}, A_{3/2}, S_{1/2}$ for transitions from the ground state to individual excited states, over a large range in Q^2 (The $A_{1/2,3/2}$ amplitudes represent the transverse couplings whereas $S_{1/2}$ describes the longitudinal coupling, respectively). These quantities can then be compared with predictions of microscopic models. Since intermediate states may carry isospin 1/2 or isospin 3/2, it is essential to measure processes in different isopin channels. For example, the single pion process may occur in four isospin configurations. In order to obtain a unique identification of the isospin of the intermediate state, three reaction channels with different isospin content have to be measured, e.g. $\gamma p \rightarrow p\pi^0$, $\gamma p \rightarrow n\pi^+$, and $\gamma n \rightarrow p\pi^-$. Measurement of the angular distributions of the final state hadrons yields information about the spin of the intermediate state. Measurement of different reaction channels allows the tagging of resonances over the entire mass range. For a complete program, in particular for the determination of small resonant amplitudes, measurement of polarization observables will be needed. These are particularly sensitive to interferences between resonant and background amplitudes, and to relative phases.

To give an idea of the potential richness of the data it is worth noting that the total amount of events we are planning to collect and analyze is of the order of 10^9. Topologies will range from single pion events to vector meson and kaon/hyperon events. I want to illustrate this program by discussing a few selected examples. In fact, many potentially very interesting physics areas that may be studied with such data have yet to be explored. More detailed information may be found in the individual proposals of the approved N^* experiments[22–30] .

3. Selected Examples of the N^* Program

3.1. $\gamma_v + p \rightarrow P_{33}(1232)$

The lowest mass state, and the dominant one at low momentum transfer is the $P_{33}(1232)$. The radiative transition from the ground state nucleon to the $P_{33}(1232)$ is

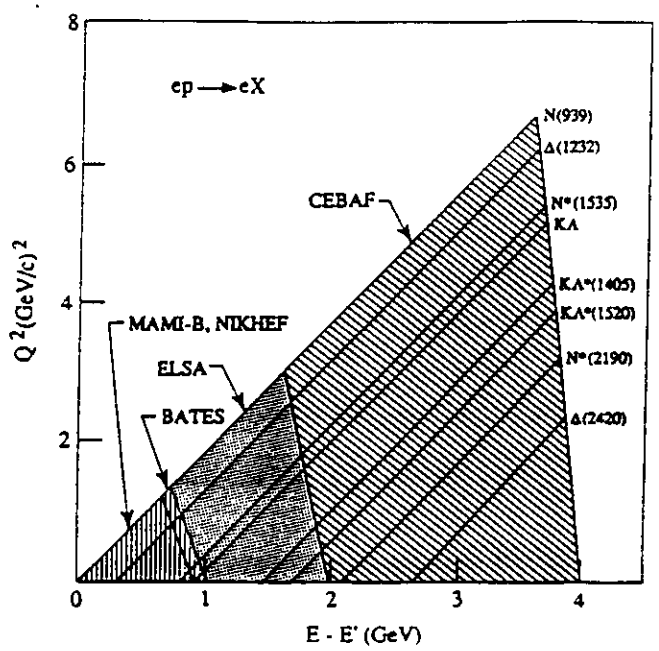

Fig. 3: Kinematical $Q^2 - \nu$ plane for a 4 GeV electron beam on a hydrogen target.

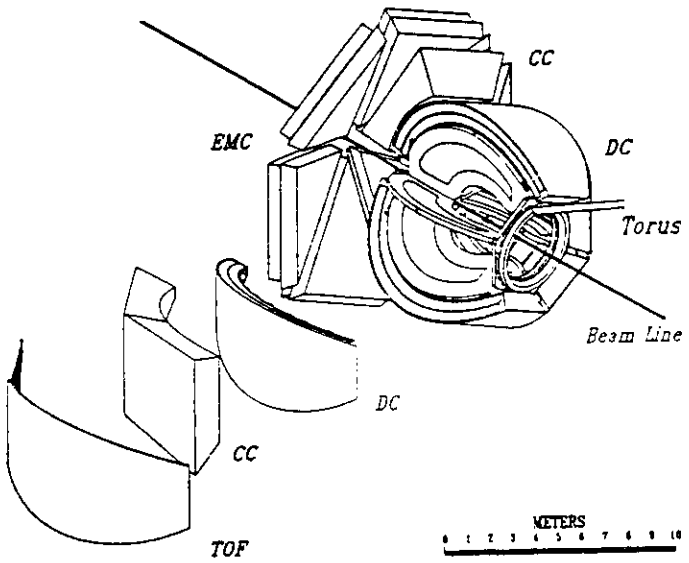

Fig. 4: The CEBAF Large Acceptance Spectrometer.[1] Six symmetrycally arranged superconducting coils generate an approximate toroidal magnetic field. Drift chambers (DC), time-of-flight counters (TOF), gas Cerenkov counters (CC), and electromagnetic calorimters (EMC) provide particle identification, tracking, and energy measurements for electromagnetically interacting particles. A field-free region around the target allows use oif polarized targets.

usually described using the electromagnetic multipoles M_{1+}, E_{1+}, S_{1+}. Quark models based on SU(6)xO(3) symmetry describe this transition as a spin flip in the $L_{3Q} = 0$ ground state, corresponding to a pure magnetic dipole transition, and thus $R_{EM} \equiv E_{1+}/M_{1+} = 0$. Non-zero values for R_{EM} may arise from a tensor force term, such as the one-gluon exchange contribution.[9] Quark models[3-5] which take into account the one-gluon exchange contribution predict the size of R_{EM} to be small for low and modestly high Q^2, and precise measurements are needed to discriminate between the various models. On the other hand, R_{EM} is expected to approach unity at very high Q^2.[21] Experimentally, R_{EM} was found to be small (Fig. 6.), in qualitative agreement with the theoretical models. Unfortunately, the data are not sufficiently accurate to discriminate against any of the dynamical models. Fig. 7 gives an impression of the statistical accuracy of existing electroproduction $p\pi^0$ data in the $P_{33}(1232)$ region, at $Q^2 = 1.0GeV^2$, where we have the most accurate data to date. Displayed is the angular distribution at fixed azimuthal angle (angle between the electron scattering plane and the nucleon-pion plane). The solid line is a fit to the data with $R_{EM} = 0$, the dashed line was generated using a value $R_{EM} = -0.05$. Obviously, the improvement expected from the proposed experiments is very significant for an accurate determination of R_{EM}.

The process $\gamma_v p \rightarrow n\pi^+$ is particularly difficult to measure with a two spectrometer setup as used in previous experiments, because the pion is emitted over the full 4π solid angle whereas the nucleon occupies a relatively small cone around the direction of the photon, and can therefore be detected more efficiently in small solid angle spectrometers. The proposed N^* measurements[22] will be the first measurements with nearly complete angular coverage, with expected statistical accuracy similar to the $\gamma_v p \rightarrow p\pi^0$ channel.

3.2. Helicity structure of $\gamma_v p \rightarrow D_{13}^+(1520)$

Much of the experimental activity in the past has concentrated on the $D_{13}(1520)$ and the $S_{11}(1535)$ states. In SU(6)xO(3), both states are members of the $\{70, 1^-\}_1$ supermultiplet. Their spatial wavefunctions are therefore expected to be identical. The electromagnetic transition to the $D_{13}(1520)$ state is often displayed in terms of the helicity asymmetry A_1, defined as:

$$A_1 = \frac{A_{1/2}^2 - A_{3/2}^2}{A_{1/2}^2 + A_{3/2}^2}$$

A_1 is insensitive to the spatial wavefunction, but rather probes the helicity-structure of the transition. One of the early successes of the quark model has been the prediction[2] that this asymmetry should switch from -1 at the photon point, corresponding to helicity 3/2 dominance, to $A \simeq 1$ for large Q^2 , corresponding to helicity 1/2 dominance. This is indeed what the data show (Fig. 8). For a detailed comparison with model calculations, more accurate, and more complete data are needed. For neutron targets, only photoproduction data are available. Note that the sensitivity to different model assumptions is different for neutrons and protons. Also, the zero crossing for neutrons is predicted to occur at higher Q^2. The proposed measurement will improve significantly

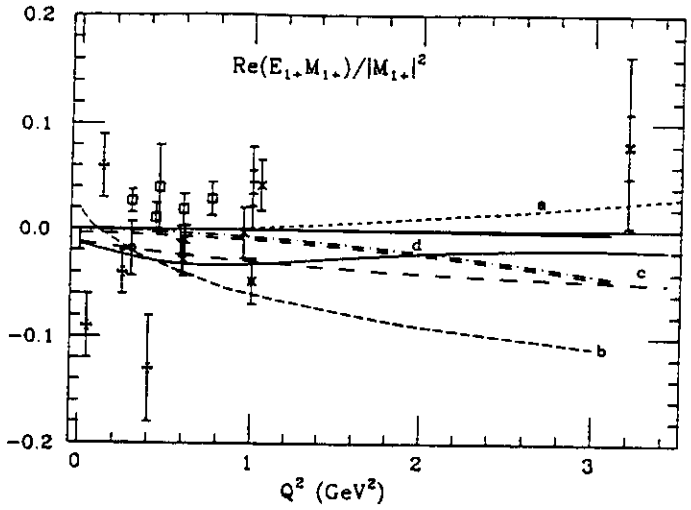

Fig. 6. R_{EM} for the $\gamma_v N P_{33}(1232)$ transition.

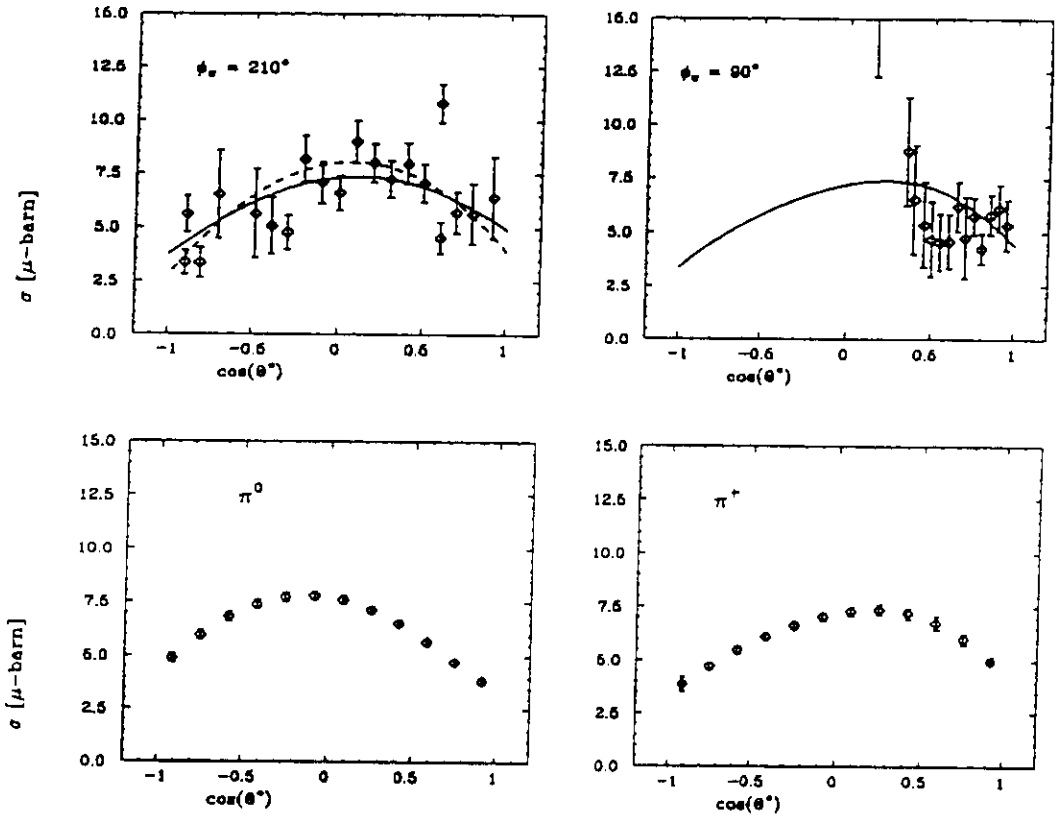

Fig. 7: Data on $\gamma_v p \to p\pi^0$ and $\gamma_v p \to n\pi^+$. The bottom graph shows the expected statistical error of the N^* proposal, assuming a luminosity of $10^{34}\text{cm}^{-2}\text{sec}^{-1}$, and a 1000 hrs data taking run. The data shown represents 2 bins out of 1000 covering the entire $P_{33}(1232)$ region and the full Q^2 range.

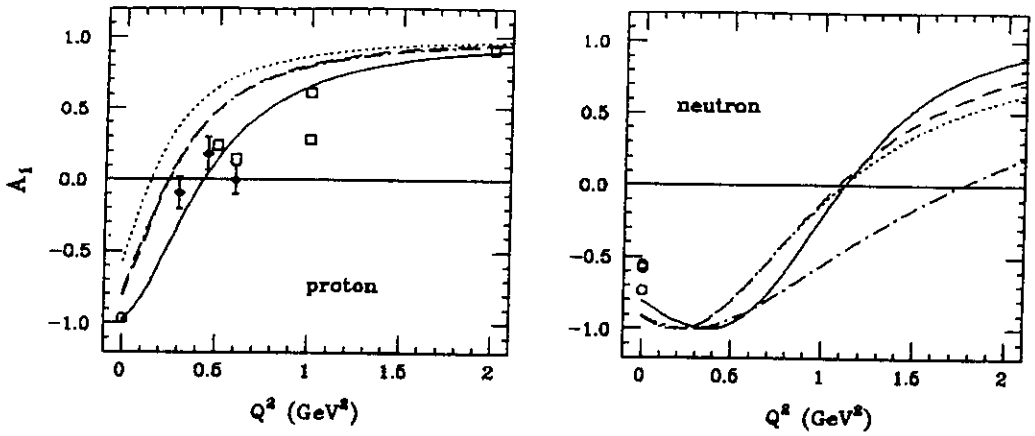

Fig. 8: Data on $\gamma_v p \to D_{13}(1520)$. Theoretical calculations from Capstick.[3]

the accuracy of the proton data and will give the first detailed electroproduction results on neutron targets.[23]

3.3. Helicity amplitude of $\gamma_v p \to S_{11}^+(1535)$

The most complete data set has been collected from the $S_{11}^+(1535)$. This state has a very large decay width to the ηN. It was also[18,19] found that the s-wave is completely dominanted by resonance production in the mass region of the $S_{11}(1535)$. This channel was therefore used to determine the transition amplitudes into this state.

Fig. 9 shows the transverse photocoupling amplitude for the $S_{11}^+(1535)$. It appears that this transition is particularly sensitive to relativistic effects; the slow falloff at high Q^2 could only be reproduced by including relativistic effects. Warns[5] found that the absolute normalization and the Q^2 dependence are sensitive to the specific parametrization of the confinement potential. These findings lend credibility to the idea that by measuring many resonance transition amplitudes one gains insight into aspects of the quark and gluon confinement. We are planning to use the ηp and possibly the η'p channel as an isospin filter to separate N^* from Δ^* states.[24,30] The higher $P_{11}(1710)$ with a large η decay width should be especially and clearly accessible in this channel. Should any of the high mass baryon states decay significantly into the $p\eta'$ channel, we may learn something about the gluonic content of such states by measuring the η' channel. Fig. 10 illustrates the improvement anticipated for the ηp channel which will give much enhanced sensitivity to contributions from higher partial waves. Again, only one sample bin out of a total of 500 is shown, covering the entire $S_{11}(1535)$ and $P_{11}(1710)$ mass region.

3.4. Test of the spin-flavor structure of quark models

Fig. 11 shows the ratio of the helicity 1/2 amplitudes for the $D_{13}^+(1520)$ and the $S_{11}^+(1535)$ in comparison with quark model calculations. Improved data for both states would provide a much better constraint on the spin structure of the transition. An

spread of 10^{-4} and an unnormalized emittance of $2 \cdot 10^{-9}$ m at 1 GeV and above. Such beam quality needs to be preserved when there is simultaneous FEL operation. These issues were successfully treated in a previous paper; see [12].

Beam Transport

The FEL electron beam from the CEBAF injection linac must be separated from the nuclear physics beam and transported into the wiggler inside the IR FEL optical cavity with appropriate optical matching. To match the wiggler focusing strength, the ~50 MeV FEL beam must be focused to a 0.3 mm radius spot at the wiggler. With a normalized beam emittance of 15 mm-mrad, this implies fairly strong focusing to $\beta^* \approx 1.0$ m at the wiggler. Small or zero dispersion is also needed.

The transport begins after the injection linac accelerating cryomodules, where the nuclear physics beam is at 45 MeV, and the FEL beam from the 10 MeV injector is at the higher energy of 50 MeV. A bending magnet displaces both beams from a linear transport, with the FEL beam bent at 11.5°. At 1.2 m downstream, where the beams are separated by 2.5 cm, the FEL beam enters a septum dipole which bends the FEL beam back by -23° to the opposite side of the injector line. A 4 m transport containing three quads for dispersion correction carries the FEL beam to a third dipole where the beam is bent 11.5° toward the wiggler. A 3.5 m transport containing four quads matches the beam into the wiggler. The matching conditions chosen in this example are $\beta_x^* = \beta_y^* = 1.0$ m at the wiggler center. Figure 7 shows beam transport accommodates a 20 m optical cavity centered on the wiggler. Fine tuning of the vertical focusing can provide matching to the wiggler focusing (matched $\beta_y^* = 0.5$ m with $K = 1.76$). At these parameters the electron beam is much smaller than the optical beam. Therefore, the focusing could be significantly relaxed without degrading FEL gain; FEL performance will not require precise electron beam optics.

The wiggler would be followed by a bending magnet and a couple of focusing quads which guide the FEL beam into a beam dump. The beam dump is designed to accept the 60 kW output of a full-intensity IR FEL beam.

The nuclear physics beam continues outside the septum to reach a separate dipole,

which returns the nuclear physics beam to the injector line to continue toward the North Linac. The resulting dogleg does not greatly affect the nuclear physics betatron functions, but does introduce an M_{56} of ~ -0.2 m, which can be compensated in the North Linac injection chicane.

The UV FEL beam transport must accommodate three functions: it must separate the FEL bunches from the nuclear physics bunch trains, it must provide longitudinal compression of the FEL bunch, and it must provide a phase-space match into the wiggler. The entire system must fit within the North Linac tunnel.

To permit energy separation of the FEL beam from the nuclear physics beams, the FEL bunches are phased 25° off the crest of the rf wave, generating a 10% energy offset. The FEL beam is at 400 MeV at the end of the North Linac, with the first-turn nuclear physics beam at 445 MeV. This difference is used to separate the beams, while the off-crest operation places an energy tilt in the FEL bunches which is used to obtain compression. The beam transport must also match the beam to the optical mode within the wiggler (2σ spot size of 300 μm, which implies $\beta^* \approx 1$ m), with adequate momentum acceptance ($\sim \pm 0.005$).

The relatively stringent transport specifications have led to a modular, achromatic, and nominally isochronous beamline design. A cross-sectional view of the tunnel at the wiggler is shown in Figure 8. The FEL beam is separated from all nuclear physics beams by the common dipole at the front end of the east arc spreader. Beam transport elements produce vertical, then horizontal, translations away from the linac axis, followed by modules for bunch compression and matching into the wiggler. We now describe each of these systems in order.

From the 10% energy offset, the FEL beam will be vertically offset from the nuclear physics beam by over 10 cm at the first independent dipole of the lowest-energy recirculation arc. This is adequate for the introduction of a quadrupole doublet to control the betatron envelopes of the 400 MeV FEL beam. After the quadrupole doublet, the FEL beam is bent onto a trajectory parallel to the linac axis, vertically displaced by 2 m. At this point, the beam is directed towards the lowest-energy east arc, is vertically dispersed

with zero dispersion slope, and has a negative path-length variation with momentum. To avoid the east arc while remaining in the tunnel, a horizontal translation away from the linac axis is required. This translation introduces a horizontal dispersion. To avoid the complication of two-dimensional dispersion matching and to correct simultaneously the path-length dependence on momentum, a phase-space rotator is introduced to transform the (negative) vertical dispersion at the end of the vertical translation into a (positive) horizontal dispersion at the beginning of the required horizontal translation. The horizontal translation is generated using a dipole geometry identical to that of the vertical, and a quadrupole triplet is introduced for dispersion suppression; the resulting combined horizontal/vertical translation is achromatic and nearly isochronous.

The phase-space rotator consists of a single quadrupole followed by a solenoid. The quadrupole and the solenoid transform the vertical angular divergence into a horizontal dispersion with zero slope. The required solenoid strength is given by the following condition:

$$\int Bdl = \pi(B\rho)$$

For a 400 MeV beam, this requires a field integral of 42 kG-m. We use a relatively long solenoid of 4 m, with a moderately long focal length $(B/(2B\rho))^{-1}$ of about 2.5 m. (Other phase-space rotators based on skew quadrupoles have been designed but are operationally more complex and appear less cost-effective.)

Immediately following the horizontal translation, a quadrupole doublet is introduced for the purpose of controlling beam envelopes in both transverse planes. After this matching doublet, a bunch compression module based on a symmetric two-doublet insertion with an embedded horizontal three-dipole chicane provides an achromatic variation of path length with momentum without modification of incident or extracted betatron functions. By modifying the excitation of the chicane, a range of -1 m $\leq M_{56} \leq$ 0 m can be produced. This is adequate to generate the desired bunch compression.

A betatron telescope consisting of a pair of quad doublets then provides matching to the wiggler across a final dispersion-suppressed vertical transverse translation. This final

translation onto the axis of the wiggler and optical cavity is a 0.5 m offset provided to ensure the optical beam clears all beam transport equipment. The final matching telescope can be tuned to provide a range of matching conditions. We have investigated the cases of upright ellipses with either $\beta^{\text{wiggler}} = 1$ m or $\beta^{\text{wiggler}} = 4$ m in both transverse planes at the center of a 3 m, 50 period wiggler. Figure 9a presents rms beam spot sizes though the system for a quasi-isochronous (no compression) case with the anticipated initial emittances of 2×10^{-8} m-rad in either plane, and a final match to upright ellipses with $\beta^{\text{wiggler}} = 1$ m at the center of the wiggler, in both planes. Dispersions are shown in Figure 9b.

Following the wiggler, spent beam is transported to a beam dump in the North Linac tunnel stub.

IV. Conclusion

A realizable design for the transport systems to the IR and UV FEL has been achieved. Component requirements have been identified and all transport elements designs can be easily achieved. Development of this hardware is proceeding at a pace consistent with CEBAF's prime mission and the availability of funds. A FEL user facility has been designed for industrial research and technology development and industry has offered \$9M of in-kind contributions to support technology development at this facility. The Commonwealth of Virginia has also pledged \$5M in matching funds and a proposal to DOE is pending.

Table 1

FEL Injector Specifications

Beam energy	10 MeV
Microbunch repetition rate	7.485 MHz
Charge per microbunch	120 pC
Average beam current	900 μA
Bunch length (4σ)	2 ps
Normalized emittance $(\epsilon_n)^{a)}$	< 15 mm-mrad
Longitudinal emittance	50 keV-degrees

a) $\sigma_x = \sqrt{\beta_x \epsilon_n / \gamma}$

Figure Captions

Figure 1 The CEBAF Front End with the recirculation system installed.

Figure 2 Recent performance of the CEBAF cavities. The gradient quoted is the actual operating gradient. No field reduction is required with beam operation.

Figure 3 FEL injector and nuclear physics beam bypass (dimensions in cm).

Figure 4 Beam transport functions $(\beta_x, \beta_y, \eta_x)$ from the exit of the CEBAF injector cryounit to the first cryomodule entrance are shown. They are calculated using DIMAD [4] with parameters from a PARMELA [5] simulation as input.

Figure 5 Macroparticle distributions from a PARMELA simulation of the FEL injector followed by the two cryomodules ($E_e = 10$ MeV). *Upper left*: distribution in longitudinal phase $(\phi, \Delta E)$. *Upper right*: density projection in energy (ΔE), showing energy spread. *Lower left*: density in longitudinal phase ϕ, showing phase spread; the 2 ps beam width is indicated.

Figure 6 Cutaway view of 500 kV gun structure. In operation, the HV sections will have corona protection and be in a SF_6 tank.

Figure 7 Plot of the beam transport functions (β_x, β_y, η) for the IR FEL. The 1.5 m IR wiggler is at the end of the transport line.

Figure 8 Cross-sectional view of the CEBAF accelerator tunnel in the east arc spreader region showing the location of the UV wiggler.

Figure 9a Horizontal and vertical rms spot sizes (σ matrix elements σ_x and σ_y) through transport system, from linac to wiggler center. Uncoupled unnormalized initial emittances $\epsilon_x = \epsilon_y = 2 \times 10^{-8}$ m-rad were assumed, the initial phase ellipses were assumed upright with $\beta_x = 5$ m and $\beta_y = 50$ m, and the final match is to upright phase ellipses with $\beta_x^{\text{wiggler}} = \beta_x^{\text{wiggler}} = 1$ m at the center of the 3 m, 50 period wiggler. Solid lines indicate

the horizontal, and dashed lines the vertical, spot size; bold lines indicate beam size with $\sigma_{\delta p/p} = 0$ (dispersive effects neglected); light lines indicate beam size with the anticipated $\sigma_{\delta p/p} = 2 \times 10^{-3}$.

Figure 9b Horizontal and vertical dispersions through transport system, from linac to wiggler center. Transport and matching conditions are as before; solid lines represent horizontal, and dashed vertical, dispersion.

References:

[1] C. Leemann, to be published in *Proceedings of the XVth International Conference on High Energy Accelerators*, Hamburg (1992).

[2] G. R. Neil *et al.*, Nucl. Instrum. Methods **A318**, 212 (1992).

[3] C.-C. Shih and S.-M. Shih, Nucl. Instrum. Methods **A304**, 788 (1991).

[4] R. V. Servranckx, K. L. Brown, L. Schachinger, and D. Douglas, "User's guide to the program DIMAD," SLAC Report 285 UC-28(A), 1985.

[5] L. M. Young, computer code PARMELA, software copyright 1991, unpublished.

[6] S. N. Simrock *et al.*, in *Proceedings of the 1990 European Particle Accelerator Conference.*

[7] C. Reece, to be published in *Proceedings of the XVth International Conference on High Energy Accelerators*, Hamburg (1992).

[8] P. Liger, G. A. Krafft, and D. Neuffer, "A Bunching Scheme for FEL Applications at CEBAF," in *Proceedings of the XIV International FEL Conference* (Santa Fe, 1991).

[9] C. Sinclair, "A 500 kV Photoemission Electron Gun for the CEBAF FEL," *ibid.*

[10] L. S. Cardman and D. Engwall (University of Illinois), private communication.

[11] R. McDonald, private communication.

[12] J. Bisognano *et al.*, Nucl. Instrum. Methods **A318**, 216 (1992).